Efficient rejection of scattered light enables deep optical sectioning in turbid media with low-numerical-aperture optics in a dual-axis confocal architecture

Jonathan T. C. Liu
Stanford University
Department of Electrical Engineering
Ginzton Laboratory
and
School of Medicine
James H. Clark Center for Biomedical Engineering
and Science
Stanford, California 94305

Michael J. Mandella
Stanford University
Department of Electrical Engineering
Ginzton Laboratory
Stanford, California 94305

James M. Crawford
University of Florida
Department of Pathology, Immunology and
Laboratory Medicine
Gainesville, Florida 32610

Christopher H. Contag
Stanford University
School of Medicine
James H. Clark Center for Biomedical Engineering
and Science
Stanford, California 94305

Thomas D. Wang
University of Michigan
Department of Internal Medicine
Ann Arbor, Michigan 48109

Gordon S. Kino
Stanford University
Department of Electrical Engineering
Ginzton Laboratory
Stanford, California 94305

Abstract. Miniature endoscopic microscopes, with subcellular imaging capabilities, will enable *in vivo* detection of molecularly-targeted fluorescent probes for early disease detection. To optimize a dual-axis confocal microscope (DACM) design for this purpose, we use a tabletop instrument to determine the ability of this technology to perform optical sectioning deep within tissue. First, we determine how tissue scattering deteriorates the diffraction-limited transverse and vertical responses in reflectance imaging. Specifically, the vertical response of a DACM to a plane reflector is measured at various depths in a scattering phantom and compared with diffraction theory and Monte Carlo scattering simulations. Similarly, transverse line scans across a knife-edge target are performed at various depths in a scattering phantom. Second, as a practical demonstration of deep-tissue fluorescence microscopy that corroborates the findings from our scattering experiments, 3-D fluorescence images are obtained in thick human gastrointestinal mucosal specimens. Our results demonstrate efficient rejection of scattered light in a DACM, which enables deep optical sectioning in tissue with subcellular resolution that can distinguish between normal and premalignant pathologies. [DOI: 10.1117/1.2939428]

Keywords: laser scanning confocal microscopy; fluorescence imaging; Monte Carlo; *in vivo* imaging; tissue phantom; three-dimensional microscopy; optical sectioning.

Paper 07429R received Oct. 22, 2007; revised manuscript received Dec. 9, 2007; accepted for publication Jan. 21, 2008; published online Jun. 11, 2008.

1 Motivation and Background

The potential utility of a miniature optical-sectioning microscope for biological investigation, preclinical animal studies, and clinical use has been well appreciated and described in the literature.[1–9] Our group is developing a miniature dual-axis confocal microscope (DACM) that can be deployed through the instrument channel of an endoscope to detect precancerous lesions in the human gastrointestinal tract. In particular, a near-IR fluorescence device is being constructed to enable speckle-free imaging of molecularly targeted reagents deep within the mucosal layer of the esophagus, stomach, and colon. In the development of this instrument, we seek to obtain a spatial resolution of a few micrometers in all three directions, and deep tissue penetration, which is desirable for the precise delineation of tumor margins through full-thickness epithelium. In this paper, we address a void in the literature by experimentally characterizing the ability of a DACM to image deeply within tissue. A tabletop DACM is used to investigate the deleterious effects of tissue scattering by imaging reflective targets in a reproducible tissue phantom.

Address all correspondence to Jonathan Liu, Stanford University Ginzton Labs, Box N-123, 450 Via Palou, Stanford, CA 94305; Tel: 650–723–2729; Fax: 650–725–3890; E-mail: jonliu@stanfordalumni.org

1083-3668/2008/13(3)/034020/11/$25.00 © 2008 SPIE

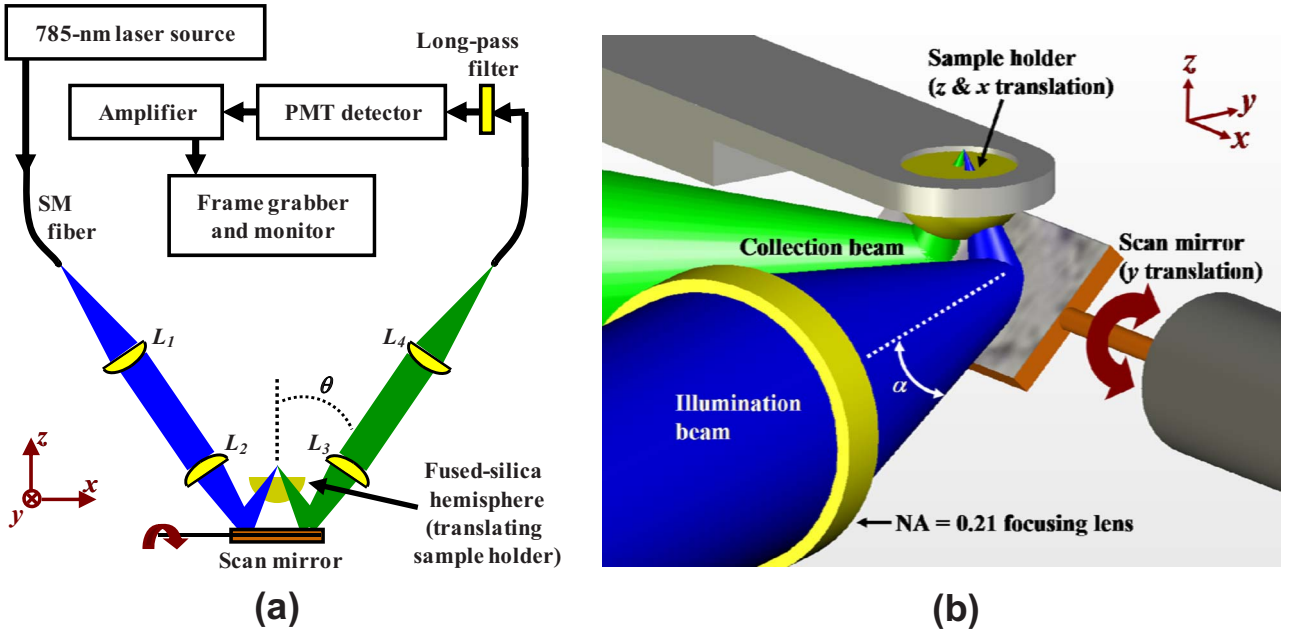

Fig. 1 DACM design. Two low-NA (α=0.21 radians) focused beams intersect at a 30 deg half-angle θ with laser illumination at 785 nm and off-axis collection of fluorescence. A galvanometric scan mirror provides fast-axis (950-Hz) scanning of the beams in the *y* direction. A hemispherical sample holder is translated with a piezo actuator in the *z* direction for vertical sectioning at 2 frames/s. Volume imaging is accomplished by translating the sample holder in the *x* direction at 1 μm/scan (2 μm/s). (a) Simplified schematic of the entire optical circuit and (b) 3-D design drawing of the scan head. The beams, originally oriented horizontally in the *x*-*y* plane, are reflected perpendicularly by the scan mirror for imaging in the vertical *z* direction.

We also provide examples of deep 3-D fluorescence image sections of *ex vivo* gastrointestinal mucosa.

The inspiration for our DACM design was provided by a method to achieve improved resolution through off-axis illumination and collection of light with high-numerical-aperture (NA) objectives.[10–12] Later, low-NA optics were proposed as a method to achieve a long working distance and a large field of view.[13] More recently, we have shown that a dual-axis architecture may be fiber coupled and combined with postobjective scanning to provide scalability of the design to millimeter dimensions.[9,14] Because the vertical response of the DACM is determined by the overlap of the input and output beams, this configuration exhibits an improved axial (vertical) sectioning response that is comparable to the transverse response.[15] Furthermore, in the dual-axis configuration, it is more difficult for light randomly scattered from the path of the input beam to be collected from the output beam, especially if the NA is small. This was investigated previously through Monte Carlo scattering simulations, indicating superior rejection of scattered light using the DACM as compared to a conventional single-axis confocal microscope.[16]

Until now, there have been no quantitative experimental studies of the optical-sectioning performance of the dual-axis confocal architecture in turbid media. While our final goal is to develop a 3-D fluorescence device for speckle-free molecularly targeted disease detection, a mirror-reflectance model is chosen as a well-established and repeatable method for quantifying the sectioning performance of the dual-axis confocal architecture in scattering media. Reflectance and fluorescence imaging are physically different in a number of ways. However, one can assume that the fundamental spatial-filtering mechanism of the DACM, for rejecting out-of-focus scattered light, is similar in both cases. For fluorescence microscopy, an analogous mirror model is difficult to realize in practice, and computationally challenging to simulate. Furthermore, such results would not enable relevant comparison with the many published studies of optical-sectioning technologies that explore reflectance mirror models.[17–19]

In this paper, we experimentally investigate the ability of dual-axis confocal microscopy to reject background scattering by measuring the axial response to a plane mirror embedded in a scattering phantom. Diffraction theory calculations (no scattering) and Monte Carlo scattering simulations (ignoring diffraction) are used to validate these experimental results. Transverse line scans of a chrome-on-glass knife-edge in turbid media are also presented to study how image contrast deteriorates due to scattering. Finally, as a practical demonstration of fluorescence imaging in tissue with a DACM, we provide 500-μm-deep fluorescence images of thick gastrointestinal mucosal specimens. The images corroborate the observations from our reflectance studies in turbid media that FWHM spatial resolution is preserved deep into tissue and that image contrast deteriorates quickly at the point where background scattering overwhelms the ballistic signal from unscattered photons.

The DACM utilizes low-NA (0.21) optics and an inexpensive low-power diode laser source for imaging deep within biological tissues (Fig. 1). Near-IR excitation of fluorescence at 785 nm is used to minimize tissue absorption and scattering for deep penetration, as well as to minimize the autofluorescence background. Aberration-free postobjective scanning of the illumination and collection beams is possible due to the long working distance afforded by the low-NA lenses, as well

as the use of a hemispherical index-matching sample holder (Sec. 2.1), enabling a large field of view to be scanned. Unlike single-axis confocal microscopes, in which the diffraction-limited axial resolution is generally much inferior to transverse resolution for a given objective-lens NA, the DACM produces a diffraction-limited focal volume that is relatively balanced in all three spatial dimensions.

2 Experimental Methods

2.1 *Dual-Axis Optical Setup*

A schematic of the DACM is shown in Fig. 1. Corning HI 780 fiber is utilized for single-mode (SM) transmission of laser and fluorescence radiation. The fiber-coupled laser is a SM diode source from Micro Laser Systems, Inc. (SRT-F785S-36) with a maximum output power of 25 mW. The laser radiation passes through a fiber-coupled optical isolator from Optics for Research to suppress back-reflections. The maximum laser power transmitted through the isolator is 15 mW. For imaging, the laser power is reduced to a maximum incident power of 1 mW on tissue samples.

Two low-NA Gaussian beams are configured to intersect at their focus with a crossing half-angle θ of 30 deg (Fig. 1). The beams are focused into the sample medium with a half-angle α of 0.21 rad, where the angle α is defined with respect to the lens aperture and in the sample medium. Lenses L_1 and L_4 have a focal length of 30 mm and a clear aperture of 9 mm. Lenses L_2 and L_3 have a focal length of 20.3 mm and a clear aperture of 8.53 mm. The $1/e^2$ intensity NA of our SM fiber (Corning HI 780) at 785 nm is 0.11 (mode field diameter=4.6 μm).

A solid immersion lens[20] consisting of a fused silica ($n=1.45$) hemisphere is used for index matching of the illumination and collection beams into tissue ($n\sim1.4$). The wave front curvature of the focused beams is matched to the curved surface of the hemisphere as it crosses the air-glass interface, thus minimizing the spherical aberration, coma, and astigmatism that would otherwise be introduced by a flat optical interface at the tissue surface[15] (i.e., flat glass window). The hemisphere also preserves the focusing half-angle α and the incident angle θ of the beams, thereby increasing the effective NA in tissue by a factor of $n\sim1.4$ (from 0.21 to 0.29). The flat surface of the hemisphere acts as a 5-mm-diam circular sample holder that is translated in z for vertical sectioning and translated in x for volume scans. An analysis of wave front aberrations due to dual-axis beam scans in x and y, through a similar index-matching optic, was performed previously,[21] indicating a maximum difference in wavefront aberration of only 0.30λ over a 600-μm horizontal field of view.

For the reflectance experiments in turbid media, the collection fiber is connected directly into a powermeter (EXFO PM-1100). The filter, photomultiplier tube (PMT), amplifier, and frame grabber are only used for raster-scanned fluorescence imaging of tissues.

2.2 *Measuring the Axial and Transverse Response in Turbid Media*

2.2.1 *Intralipid scattering phantom*

Among the most widely used and well-studied tissue phantoms for optical imaging are lipid emulsions similar to milk.

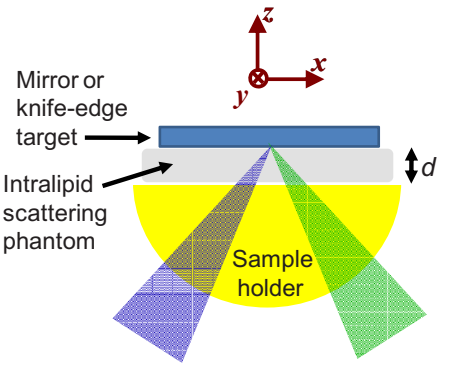

Fig. 2 Close-up view of the sample stage for mirror reflectance studies in a scattering phantom (Intralipid). The thickness of the scattering phantom is given by d. Axial mirror scans are performed by translating a plane reflector in the z direction. Transverse line scans are performed by translating a chrome-on-glass knife-edge target in the x direction.

In these studies, 20% Intralipid is used (Baxter Healthcare Corp). Approximate values for the optical properties of Intralipid can be found in the literature.[22] For our studies, the scattering coefficient μ_s is measured directly during each experiment. The absorption coefficient μ_a is negligible, and the anisotropy g (defined in Sec. 2.2.3), is assumed to be 0.75 in our simulations, based on results reported in the literature. Vigorous stirring of the Intralipid solution prior to use results in consistent measurements of μ_s.

2.2.2 *Axial mirror and transverse knife edge scans*

A piezoelectric stage (Physik Instrumente P-783.ZL) translates the dual-axis microscope's hemispherical index-matching sample holder in the z (axial) direction. A plane mirror is held at calibrated distances above the sample holder and is translated with a high-resolution (±0.1 μm) piezoelectric scanner (Physik Instrumente P-762.ZL).

For the axial mirror scans, an Intralipid scattering phantom, or water (for zero-scatter measurements), is injected on top of the sample holder, as shown in Fig. 2. The sample holder is lowered such that the dual-axis focus is located at a precalibrated distance above the flat surface of the sample holder. Then, the silvered mirror is lowered into the Intralipid media until a peak signal is found, indicating the position ($z=0$) at which the mirror is at the focal plane of the dual-axis microscope. Axial scans are performed by scanning the silvered mirror in the vertical direction. Control signals are generated in LabVIEW using a National Instruments waveform generation board (PCI-MIO-16E-1). The axial scans are performed with a linear ramp waveform at 0.01 Hz. Laser intensity signals are recorded at 10 Hz onto a memory buffer in a powermeter (EXFO PM-1100). The memory buffer is then transferred via a general purpose interface bus (GPIB, IEEE 488.2) onto a PC through a National Instruments GPIB board (PCI-GPIB) programmed with LabVIEW.

Transverse knife-edge scans are accomplished by using a piezoelectric stage (Physik Instrumente P-783.ZL) to horizontally translate a chrome knife-edge target imprinted on a glass substrate (Applied Image Group, Rochester, New York). The surface of the knife-edge target is positioned axially in the

Table 1 DACM specifications.

	Theoretical Resolution, FWHM (Point Reflector)	Theoretical Axial Resolution, FWHM (Plane Mirror Reflector)	Theoretical Focal Volume ~ $(4/3)\pi[(\Delta x/2)(\Delta y/2)(\Delta z/2)]$	Measured Resolution, FWHM
DACM $\alpha=0.21$ rad, $\theta=30$ deg	$\Delta x=1.34$ μm $\Delta y=1.16$ μm $\Delta z=2.31$ μm	$\Delta z=2.1$ μm	1.9 μm^3	$\Delta x=1.45$ μm (knife-edge response) $\Delta z=2.40$ μm (plane mirror)

focal plane of the dual-axis microscope to achieve optimal signal strength and contrast in the line scans. Intralipid, 20%, is injected in the gap (precalibrated distance) between the hemispherical sample holder and the knife-edge target for measurements through scattering media.

2.2.3 *Simulations*

Diffraction theory calculations, described previously,[15] can be used to calculate the theoretical FWHM resolution of the DACM, in response to both point and plane reflectors. Numerical integration routines are performed in MATLAB. In the dual-axis system studied here, the ratio of the aperture diameter to the $1/e^2$ Gaussian beam diameter is 1.3. Experimental parameters are $\lambda=0.785$ μm, $\alpha=0.21$ rad, $\theta=30$ deg, and $n=1.4$ (approximate index of tissue). Calculated and measured resolutions are listed in Table 1.

We performed Monte Carlo simulations on an optical model that approximates our experimental setup. As described previously,[16] a nonsequential ray optics program (ASAP® 2006, Breault Research Org.) is used to perform scattering simulations. The angular distribution of scattered light, for nonabsorbing spherical scatterers, is given by the Henyey-Greenstein phase scattering function, which is an approximation to Mie scattering theory:[23]

$$p(\theta)=\frac{1}{4\pi}\frac{1-g^2}{(1+g^2-2g\cos\theta)^{3/2}}, \quad (1)$$

where g, the anisotropy factor, is defined as

$$g=\langle\cos\theta\rangle=\int_0^{2\pi}\int_0^{\pi}(\cos\theta)\cdot[p(\theta)\sin\theta\,\mathrm{d}\theta\,\mathrm{d}\varphi]. \quad (2)$$

In these simulations, a detection "pinhole" diameter of 3 μm is chosen, which approximates the "top-hat equivalent" diameter[24] that would yield the same throughput as a Gaussian-weighted pinhole with a $1/e^2$ diameter of 4.6 μm (the mode field diameter of our SM fiber). The illumination source in the simulations is a collimated beam with a Gaussian intensity distribution that matches the beam in our experimental DACM. However, diffraction effects are not modeled in the Monte Carlo simulations.

As described in Sec. 3.1, the scattering coefficient μ_s of our Intralipid scattering phantom is measured experimentally and is the value used in our Monte Carlo simulations. The anisotropy g is estimated based on published studies.[22] Our measured values for μ_s are also consistent with published values in the literature.

2.3 *Dual-Axis Imaging of Gastrointestinal Mucosa*

2.3.1 *Volumetric scanning*

Vertical sectioning is the primary mode of imaging for our device. Postobjective horizontal (fast-y-axis) scanning is accomplished sinusoidally at 950 Hz with a galvanometric scan mirror from GSI Lumonics (VM500), and vertical (slow-z-axis) depth scanning is performed at 2 Hz with a piezotranslation stage from Physik Instrumente (P-290). The vertical waveform is a sawtooth modified with smooth turnarounds to avoid mechanical ringing. Waveforms are produced with National Instruments waveform generators programmed in LabVIEW®. Signals are displayed and stored with an 8-bit frame grabber from Data Translation (DT3152). The frame grabber is synchronized with horizontal and vertical trigger pulses supplied by the same National Instruments boards used to generate the scanning waveforms. The imaged field of view is 800 (horizontal) by 500 μm (vertical), acquired at a pixel rate of 2.26 MHz for images that are 1000 (horizontal) by 420 pixels (vertical) in size. For volumetric imaging, the sample stage is translated in the third dimension x with a computer-controlled motorized actuator from Newport Corporation (LTA-HL). Vertical images are acquired and stored at 2 frames/s, while the sample is translated in x at a constant velocity to obtain serial sections separated by 1 μm. The 2-D and 3-D images and animations are rendered with the Amira 3.0 software package.

2.3.2 *Depth-weighted fluorescence detection*

The fluorescence microscope utilizes a Hamamatsu PMT (H7422-50) and PMT controller (C8137-02) for the detection of incoherent single-photon fluorescence. A Semrock RazorEdge® long-pass filter (LP02-785RU-25) is used to reject 785-nm laser radiation prior to PMT detection. The PMT output is converted to a voltage signal with a current amplifier from FEMTO Messtechnik GmbH (DHPCA-100). The transimpedence gain of the amplifier is set to 10^6 with a corresponding bandwidth of 3.3 MHz.

A large dynamic range of fluorescence signal (>40 dB) is encountered when imaging vertical sections with deep tissue penetration. To prevent PMT detector saturation, as well as to

optimize the signal levels for acquisition with an 8-bit (24-dB) frame grabber, the PMT gain is modulated with a 2-Hz sawtooth waveform synchronized to the slow-axis waveform (vertical z scan). By adjusting the offset and amplitude of this gain-control waveform, it is possible to compensate for an exponential loss of fluorescence signal with imaging depth due to absorption and scattering losses, as well as a depth-dependent dye distribution. Due to the slow gain-settling time of the PMT (0.2 s), it is necessary to introduce a slight delay (phase shift) between the sawtooth waveforms for imaging at 2 frames/s.

2.3.3 *Tissue preparation*

Fresh tissues were collected via pinch biopsy during standard endoscopy at the Palo Alto Veterans Administration Hospital. Patient informed consent was obtained and approved by the Institutional Review Board of the Stanford University School of Medicine. Fresh biopsy specimens were soaked for 1 to 5 min in a near-IR dye from LI-COR Biosciences (IRDye® 800CW). The dye was dissolved, at a concentration of 0.1 mg/mL (90 μM), in water that contained 5% DMSO to facilitate tissue penetration. Prior to imaging, excess dye was removed by soaking and irrigating the tissues with water. After imaging with our dual-axis fluorescence confocal microscope, biopsy samples were fixed in 10% formalin and submitted for routine histologic processing [hematoxylin and eosin (H&E) staining].

3 Results

3.1 *Axial Response in Turbid Media*

As described in Sec. 2.2.2 and depicted in Fig. 2, the DACM was used to image reflected light from a plane mirror located at various depths within an Intralipid scattering phantom. Our axial mirror response experiments were all performed in a regime where the peak signal, from a mirror placed at the focus of our microscope, is dominated by ballistic (unscattered) photons. Therefore, the decay in the peak mirror signal, as a function of depth, follows Beer's law: $\exp(-2\,\mu_s d/\cos\theta)$. Here we assume that absorption effects are negligible, as compared to scattering losses. The depth of the mirror in the scattering media is given by d and the factor of 2 accounts for both the illumination and collection path lengths. For the dual-axis configuration, a factor of $\cos\theta$ is introduced due to the off-axis geometry of the dual-axis beams.

Figure 3 is a normalized plot of the measured fall-off in the ballistic signal (mirror at the focus) and the signal due to background scatter (no mirror) as a function of depth. As we can see from the plot, the peak signal is well above the background scattering level, suggesting that it is dominated (>98%) by ballistic photons reflected at the mirror surface. The scattering coefficient μ_s may be inferred from a curve fit to the peak-signal decay as a function of depth. The background signal due to scattering is measured by removing the mirror from the Intralipid phantom. Monte Carlo simulations, based on the measured value for μ_s, yield good agreement with experimental values: the ballistic signal falls off exactly according to Beer's law and the scattering background decays at the same rate as the experiments. The Monte Carlo simulation of the background scattering level is approximately 4 dB below the experimental values. This disparity is due to the fact that a SM fiber was used as the collection pinhole in our experimental DACM. Therefore, diffraction, slight optical misalignments and/or aberrations introduce losses in the peak (ballistic) signal that were not captured in the ideal diffraction-free Monte Carlo simulations.

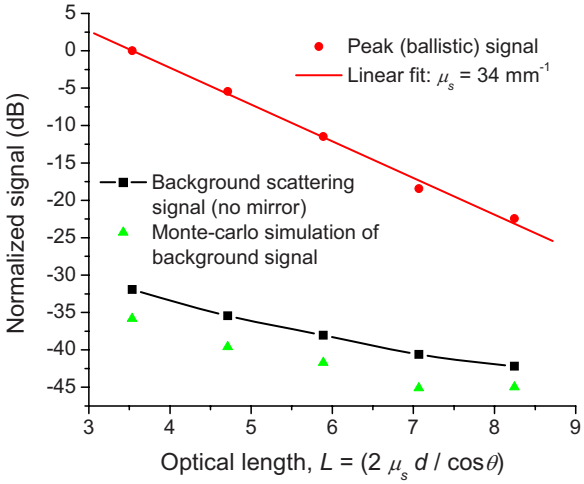

Fig. 3 Dual-axis confocal signal and scattering background versus depth. At these optical lengths, the peak signal is dominated by ballistic photons reflected from a plane mirror located at the focus of the dual-axis microscope, and exhibits a Beer's law decay (μ_s = 34 mm^{-1}) with respect to depth through scattering media. Signal due to background scatter is also measured, and predicted by Monte Carlo scattering simulations, by removing the mirror from the scattering phantom (20% Intralipid). Monte Carlo simulations ignore diffraction, alignment and aberration losses, leading to the ~4 dB discrepancy between measured and simulated scattering background levels. The optical length L gives the total number of mean free paths in scattering media traversed by the ballistic dual-axis photons along the illumination and collection route.

Axial mirror scans, from the focal plane at z=0 μm to a defocus of z=20 μm, were performed at various depths within the scattering phantom, as displayed in Fig. 4(a). Note that the near-focus axial response, primarily due to ballistic photons reflected from the mirror, remains diffraction limited until the background scattering level is approached and begins to dominate. The Monte Carlo simulations in Fig. 4(b) show good agreement with the measured results. Figure 4(b) also contains results from two diffraction-theory calculations. The first diffraction-theory calculation is of the axial response of our DACM to a plane mirror in the absence of scattering. This calculation matches the experimental curve, shown in Fig. 4(a), for an axial mirror scan in water (no scattering). The second diffraction-theory calculation in Fig. 4(b) is of the axial response of a conventional single-axis confocal microscope with the same FWHM (−3-dB) axial resolution as our DACM. The single-axis geometry yields a relatively slow fall-off in its diffraction-limited axial response ($\sim 1/z^2$) compared with the dual-axis [$\sim\exp(-kz^2)$]. More implications of these results are discussed in Sec. 4.

3.2 *Transverse Response in Turbid Media*

As described in Sec. 2.2.2, a transverse scan, of a chrome knife-edge on glass, was performed in scattering media. The

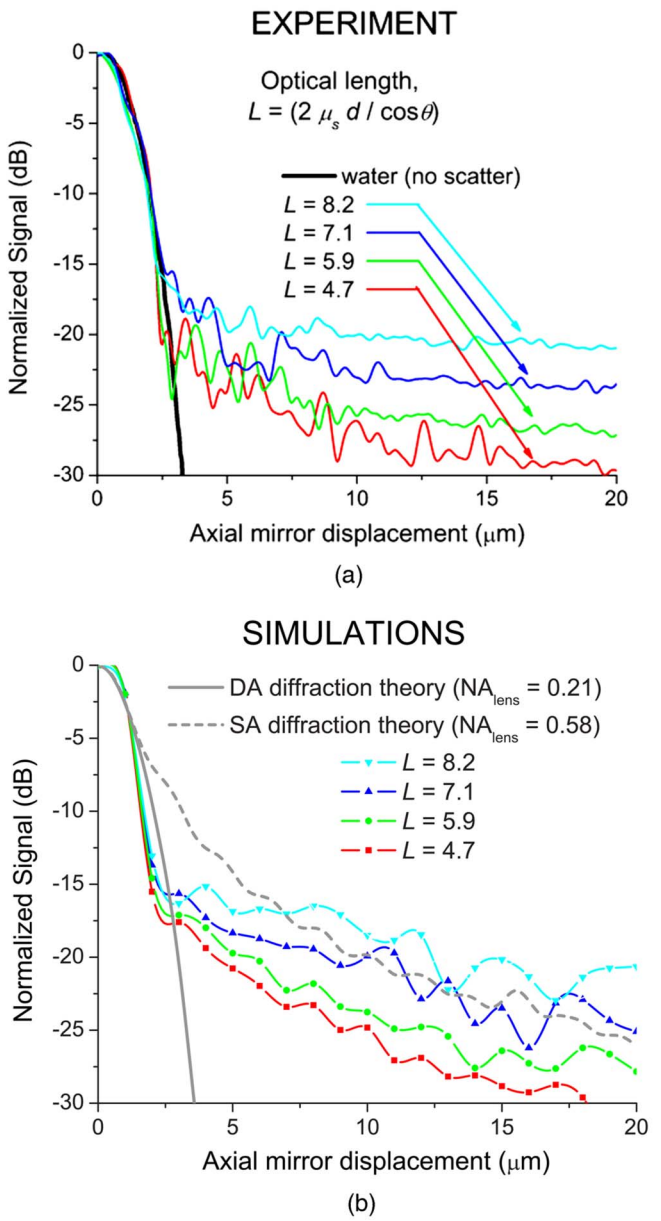

Fig. 4 Axial response of a dual-axis microscope to a plane mirror in turbid media. The measured scattering coefficient of our Intralipid scattering phantom μ_s is 34 mm^{-1}. An anisotropy of g=0.75 is assumed in the simulations. (a) Experimental measurements made with the mirror located at round-trip optical lengths of L=4.7–8.2, where $L=2\mu_s d/\cos\theta$ is the total number of mean free paths traversed by ballistic photons along the illumination and collection paths in turbid media; a μ_s=0 curve obtained by performing a mirror scan through water is also shown, and (b) diffraction theory (no scattering) and Monte Carlo simulations (no diffraction). Diffraction simulations are provided for our dual-axis confocal (NA=0.21 focusing lenses) as well as for a single-axis confocal (NA=0.21 focusing lens) with an identical FWHM (–3-dB) axial resolution.

reflectivity of chrome at 785 nm is approximately 40%, and the Fresnel reflection at a water-glass interface is ~0.4%. This 20-dB difference in reflectivity is seen in Fig. 5(a) for low levels of scattering ($L<7.5$). As the optical length L increases, the contrast in signal between chrome and glass decreases. The high reflectivity of the chrome (40%) ensures that ballistic photons reflected from that surface dominate over the scattering background. Therefore, the signal from the chrome surface obeys a Beer's law decay with respect to depth, even at L=15. The weaker signal from the glass surface, however, is increasingly dominated by the scattering background as L extends above 7.5.

In Fig. 5(a), the transverse resolution of the knife-edge line scan remains relatively constant as a function of scattering length, whereas contrast deteriorates quickly at the most extreme scattering lengths ($L\sim15$). A measurement of the 10 to 90% intensity points of the knife-edge response confirms that this quantity is constant as a function of imaging depth [Fig. 5(b)]. This is consistent with the axial mirror scan results: the FWHM (–3-dB) spatial resolution is clearly preserved regardless of imaging depth in turbid media [Fig. 4(a)]. However, contrast degrades quickly at the point where background signal due to scattering overwhelms the ballistic signal. Figure 6 shows the effect of the scattering background on the contrast between the chrome and glass surfaces of the knife-edge, where contrast is defined as

$$\text{contrast}=\frac{I_{\max}-I_{\min}}{I_{\max}+I_{\min}}. \tag{3}$$

The implications of these results are discussed in Sec. 4.

3.3 *Deep Dual-Axis Fluorescence Imaging of Gastrointestinal Mucosa*

Clearly, to demonstrate optical-sectioning performance in real tissues, axial and transverse mirror models, though quantitatively informative, are poor substitutes for images obtained in fresh biological tissues. Therefore, we present volumetric fluorescence images of gastrointestinal mucosa, as described in Sec. 2.3.1. While there is much variability in biological tissues, reported values for μ_s, for esophagus and colon at 785 nm, are approximately 7 and 20 mm^{-1}, respectively.[25,26]

3.3.1 *Diagnostic imaging of esophageal mucosa*

Mucosal biopsies from normal esophagus were imaged following dye application. A vertical section is shown in Fig. 7(a), demonstrating the ability to visualize squamous cells to a depth of 500 μm. Note that the PMT detector gain is varied during each vertical image, at 2 frames/s, to compensate for an exponential decrease in fluorescence signal with depth. A horizontal rendering at a depth of 275 μm, of 300 vertical sections spaced by 1 μm, is shown in Fig. 7(b).

Barrett's esophagus is a condition in which the normal squamous epithelium of the esophagus has been replaced by an abnormal columnar epithelium termed specialized intestinal metaplasia. Since Barrett's esophagus is often indistinguishable from normal stomach (gastric) mucosa under white-light endoscopy, biopsy and histological examination are necessary for the accurate diagnosis of this precancerous condition. Vertical and horizontal images of Barrett's esophagus, respectively, are shown in Figs. 7(c) and 7(d). Figure 7(e) shows a vertical section of a transition junction between squamous and Barrett's esophagus. A horizontal rendering, at a depth of 205 μm, is shown in Fig. 7(f) along with the corresponding histology (H&E staining) in Fig. 7(g). The presence

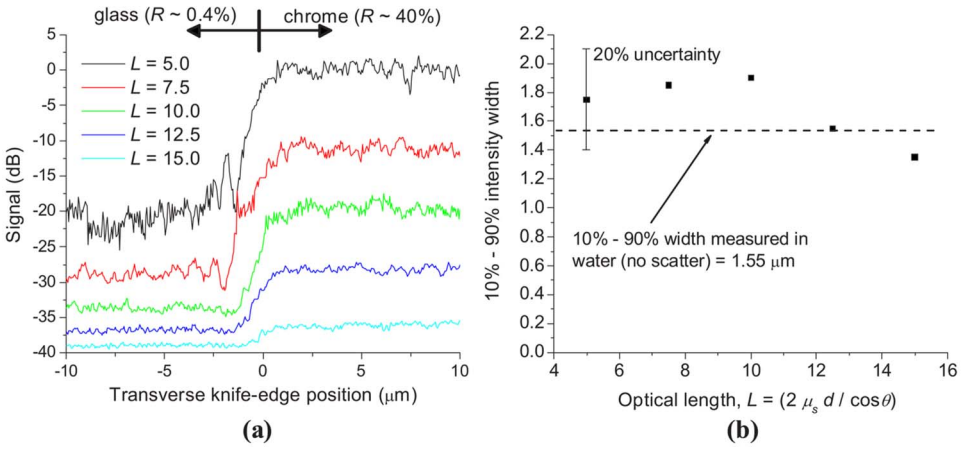

Fig. 5 (a) Transverse line scans of a chrome-on-glass knife-edge target positioned at various round-trip optical lengths, $L=2\mu_s d/\cos\theta$, in an Intralipid scattering phantom. The knife-edge surface is positioned at the focal plane of our dual-axis microscope for maximum signal and contrast. The maximum difference in signal is ~20 dB and degrades with depth as background scattered light begins to dominate. (b) Distance between the 10 to 90% intensity points in our knife-edge line scans, which remains relatively constant as a function of imaging depth in turbid media (optical length).

of mucus-secreting goblet cells, which appear as brightly stained vacuoles among the columnar cells lining the glands [Fig. 7(f)], confirms the specialized intestinal metaplasia of Barrett's esophagus rather than gastric mucosa.

3.3.2 *Diagnostic imaging of colonic mucosa*

Colonic polyps are routinely biopsied and diagnosed histologically. Adenomatous polyps are a dysplastic transformation of colonic mucosa with precancerous potential. Figure 8(a) shows a vertical section of a colonic polyp biopsy, following dye application. A horizontal rendering of this tissue, at a depth of 50 μm, is shown in Fig. 8(b), along with corresponding histology (H&E staining) in Fig. 8(c). This example of an adenoma, showing low-grade dysplasia, is easily contrasted with and distinguished from optical sections of normal colonic mucosa [Fig. 8(d)] as well as optical sections of adenoma exhibiting high-grade dysplasia [Fig. 8(f)]. The corresponding histology (H&E staining) is shown in respective order [Fig. 8(e) and Fig. 8(g)]. In normal mucosa, the crypts (glands) are circular and evenly spaced. In adenomatous mucosa, the crypts are ellipsoidal with high eccentricity and are lined with hyperproliferative and stratified colonocytes.

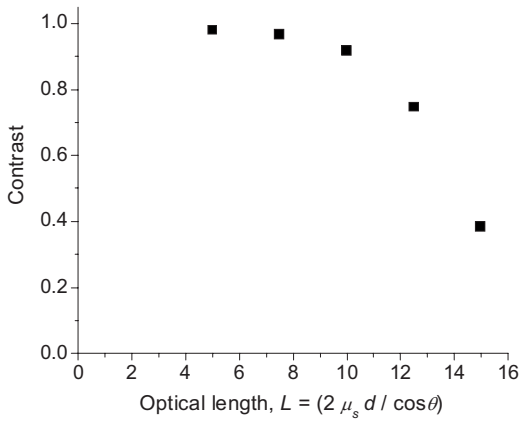

Fig. 6 Contrast in our knife-edge line scans as a function of depth. See text for details.

4 Discussion

The dual-axis confocal architecture has advantages over conventional single-axis confocal microscope designs, particularly for miniaturization and *in vivo* use. The DACM utilizes low-NA objectives, which provide long working distances and enable aberration-free postobjective scanning over a large field of view. Deep tissue microscopy requires efficient rejection of background scattering, which has been accomplished in a variety of ways and described in the literature. Among popular methods are time- and coherence-gating methods, such as optical coherence tomography, as well as nonlinear microscopy techniques, accomplished with high-power lasers and high-NA focusing. In this paper, we demonstrate that simple low-NA optics and low-power diode lasers can be utilized in a dual-axis confocal architecture to image deeply within turbid media. The DACM does not require coherent detection, thereby making it compatible with molecularly targeted fluorescence imaging that is free from speckle noise. For example, we plan to utilize a miniature endoscopic DACM to image fluorescent peptides, discovered by other researchers within our group, that preferentially bind to cell-surface molecular biomarkers of disease in the colon.[27]

To quantify the optical-sectioning performance of a tabletop DACM, simple reflectance experiments were performed that may be verified with Monte Carlo scattering simulations. We previously performed diffraction-theory calculations to show that the axial response of the DACM falls off quicker, and has a larger dynamic range, than the response of a single-axis confocal microscope with an equivalent FWHM axial resolution.[15] In this study, we show that in the vicinity of the focal plane (~20 μm), the axial response of our DACM to a plane mirror, through up to ~8 mean free paths of scattering media (round-trip optical length), is superior to the diffraction-limited (scatter-free) performance of a single-axis confocal with an equivalent FWHM axial resolution. We also

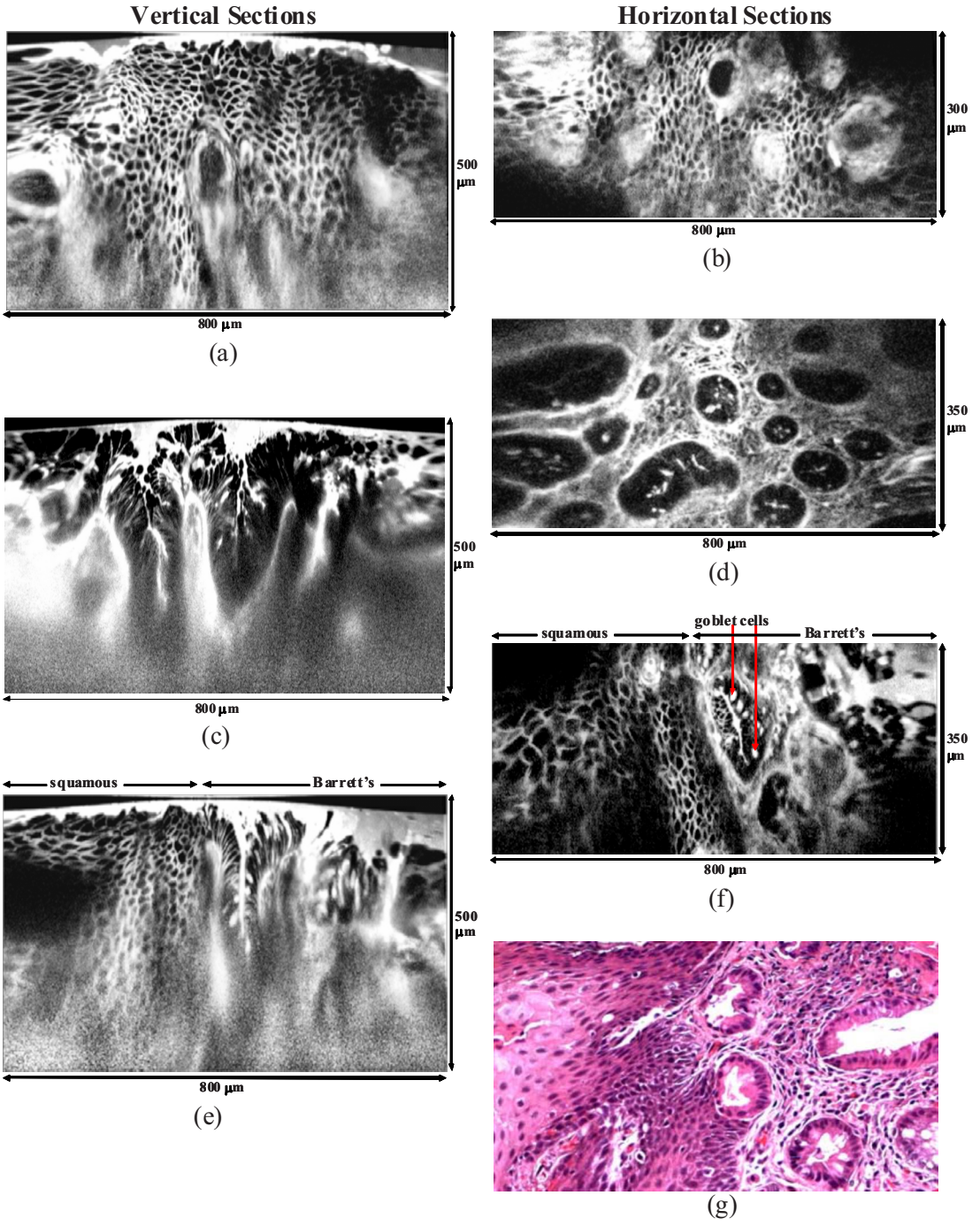

Fig. 7 Structural images of normal squamous esophagus tissue and Barrett's esophagus: (a) vertical image section of a normal squamous esophagus biopsy, (b) horizontal image section of a normal squamous esophagus biopsy, with the image at a depth of 275 μm; (c) vertical image section of a Barrett's esophagus biopsy; (d) horizontal image section of a Barrett's esophagus biopsy, with the image at a depth of 200 μm; (e) vertical image section of a biopsy showing the transition junction between squamous and Barrett's esophagus; and (f) horizontal image section of a biopsy showing the transition junction between squamous and Barrett's esophagus, with the image at a depth of 200 μm. Here the presence of mucin-secreting goblet cells, brightly stained vacuoles in these images, confirms the existence of specialized intestinal metaplasia (Barrett's esophagus). (g) A histologic section (H&E staining) of a biopsy at the transition junction between squamous and Barrett's esophagus shown for comparison with the images of thick tissues using the DACM.

demonstrate excellent contrast in transverse line scans of a knife-edge target, through round-trip optical lengths of up to $L=15$ in turbid media. Our results, presented in Secs. 3.1 and 3.2, indicate that the dual-axis confocal architecture exhibits excellent optical sectioning that is balanced in performance along both the axial and transverse dimensions.

As reported in the literature, transverse knife-edge experiments similar to ours have been carried out to study single-

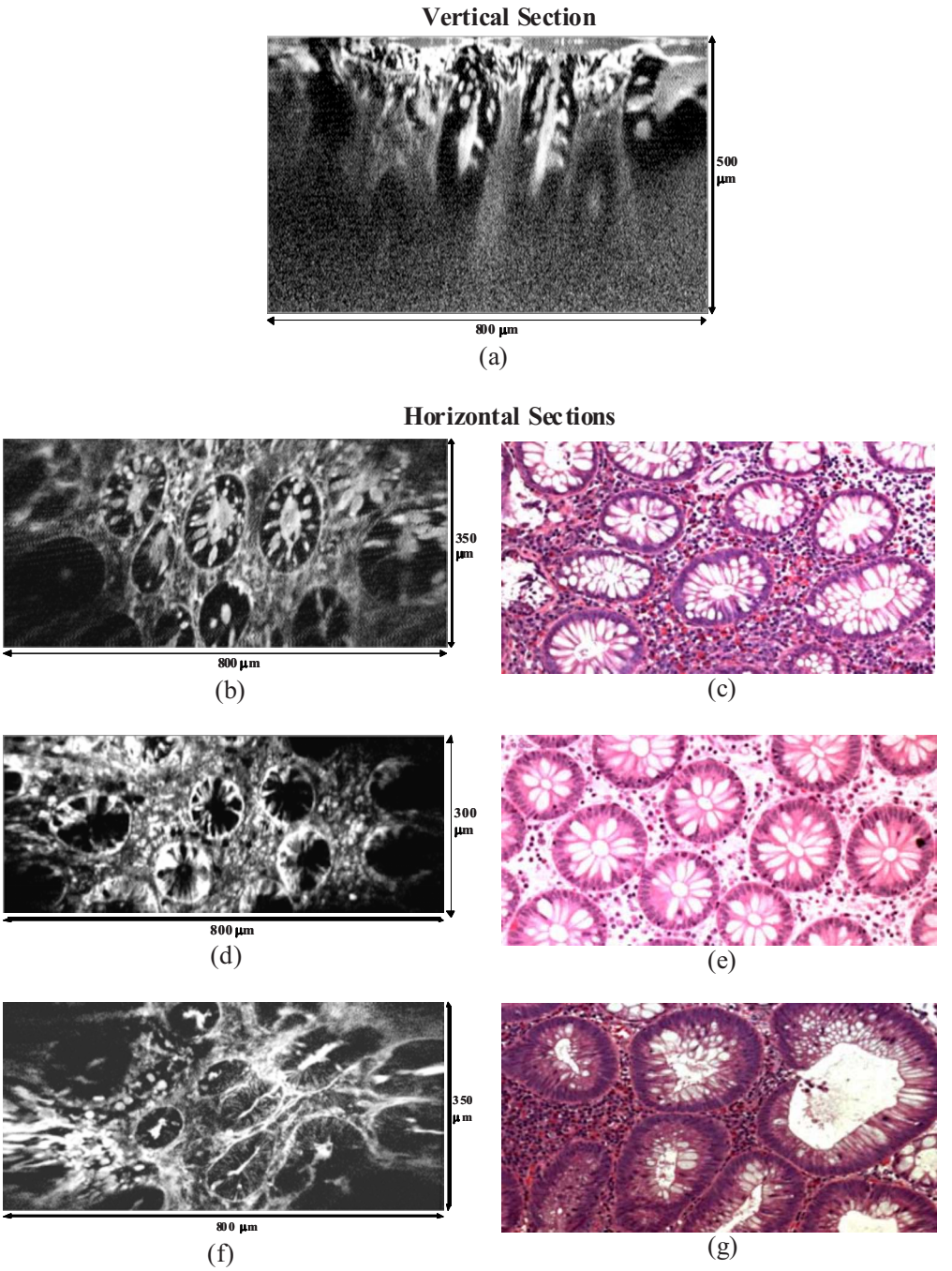

Fig. 8 Structural images of colonic mucosa: (a) vertical image section of a colonic polyp biopsy, where an adenoma with low-grade dysplasia is observed; (b) horizontal image section of a colonic polyp biopsy exhibiting low-grade dysplasia, image at a depth of 140 μm; (c) histologic section (H&E staining) of an adenomatous polyp with low-grade dysplasia, for comparison with dual-axis confocal images of thick tissues; (d) horizontal section, at a depth of 115 μm, of a normal colon biopsy, where evenly spaced, circular crypts (glands) are observed; (e) histologic section (H&E staining) of a normal colon biopsy; (f) horizontal section, at a depth of 115 μm, of an adenomatous polyp biopsy, exhibiting high-grade dysplasia, where irregular and elongated crypts are observed; and (g) histologic section (H&E staining) of an adenomatous polyp biopsy exhibiting high-grade dysplasia.

axis confocal microscopes. The most impressive results were reported by Kempe et al.[19] In that study, chrome-on-glass reflectance gratings were imaged, yielding results that are comparable to our own results shown in Fig. 6. However, those results were obtained from a confocal microscope that had an effective NA of only 0.28, which is similar to the effective NA of our DACM (Sec. 2.1). Such a confocal, in a single-axis arrangement, would exhibit an FWHM axial resolution of the order of 15 μm, not to mention an extremely slow axial response, as discussed in Sec. 3.1. It has been determined that there is a reduction in the amount of background scattered light collected by a single-axis confocal as NA is reduced, at the cost of a degradation in resolution and axial-sectioning

response.[28] Therefore, while a low-NA single-axis confocal microscope may perform well for imaging a flat "presectioned" reflective target in scattering media, the slow axial response and poor axial resolution would not enable effective optical sectioning in 3-D biological tissues. Note that our study is by no means intended as a comprehensive comparison between single-axis and dual-axis confocal microscopies. These two confocal architectures represent distinct modalities that possess strengths and weaknesses for different applications. Our primary aim was to perform experimental studies to characterize the DACM in turbid media, as has been done with single-axis confocal microscopes in the past.

Of the numerous studies of optical-sectioning technologies,[17–19,28] few studies investigate both axial and transverse performance in scattering media. Of those studies, still fewer, if any, provide a demonstration of imaging performance in actual biological tissues as well. Since mirror and knife-edge models may be misleading, we demonstrate deep 3-D fluorescence microscopy in biological tissues. Collectively, these results consistently demonstrate the deep optical-sectioning abilities of the DACM. In particular, for the reflectance studies described in Secs. 3.1 and 3.2, we observed that FWHM spatial resolution is not significantly affected by imaging depth (optical length), but that image contrast quickly degrades as the scattering background overwhelms the ballistic signal. This is also apparent in many of the images of biological tissues. For example, in Figs. 7(a) and 7(e), the membranes of the individual squamous esophagus cells remain well defined and resolvable deep into the sample, but quickly lose visibility at a certain point as the scattering background overwhelms the ballistic signal from the cell walls.

In summary, the dual-axis confocal architecture exhibits efficient rejection of scattered light, as demonstrated through quantitative mirror reflectance studies in a scattering phantom, and through imaging exogenous single-photon fluorescence contrast in human gastrointestinal biopsy samples. The results indicate the utility of this technology to distinguish cellular and morphological signatures of various pathologies such as Barrett's esophagus and colonic adenomas, as well as to distinguish between grades of colonic dysplasia. The 3-D optical-sectioning ability of the DACM enables arbitrary orientations and locations to be viewed. Thus, a miniature endoscope-compatible version of this device would provide a valuable tool for rapidly diagnosing and staging diseases, as well as for guiding surgical resection.

Acknowledgments

This work was funded in part by grants from the National Institutes of Health, including K08 DK067618 (NIDDK), U54 CA105296 (NCI), and R33 CA109988 (NCI). This work was also supported by funding through the Center for Biophotonics, a National Science Foundation Center managed by the University of California, Davis (PHY 0120999). Jonathan Liu is supported by a Canary Foundation / American Cancer Society postdoctoral fellowship for early cancer detection. We thank Shai Friedland, Roy Soetikno, Peyman Sahbaie, and Larry Wong for technical support.

References

1. J. G. Fujimoto, M. E. Brezinski, G. J. Tearney, S. A. Boppart, B. Bouma, M. R. Hee, J. F. Southern, and E. A. Swanson, "Optical biopsy and imaging using optical coherence tomography," *Nat. Methods* **1**, 970–972 (1995).
2. G. J. Tearney, M. E. Brezinski, B. E. Bouma, S. A. Boppart, C. Pitris, J. F. Southern, and J. G. Fujimoto, "*In vivo* endoscopic optical biopsy with optical coherence tomography," *Science* **276**, 2037–2039 (1997).
3. B. E. Bouma and G. J. Tearney, *Handbook of Optical Coherence Tomography*, Marcel Dekker, New York (2002).
4. M. T. Myaing, D. J. MacDonald, and X. Li, "Fiber-optic scanning two-photon fluorescence endoscope," *Opt. Lett.* **31**, 1076–1078 (2006).
5. K. Carlson, M. Chidley, K.-B. Sung, M. Descour, A. Gillenwater, M. Follen, and R. Richards-Kortum, "In vivo fiber-optic confocal reflectance microscope with an injection-molded plastic miniature objective lens," *Appl. Opt.* **44**, 1792–1797 (2005).
6. R. Kiesslich, J. Burg, M. Vieth, J. Gnaendiger, M. Enders, P. Delaney, A. Polglase, W. McLaren, D. Janell, and S. Thomas, "Confocal laser endoscopy for diagnosing intraepithelial neoplasias and colorectal cancer in vivo," *Gastroenterology* **127**, 706–713 (2004).
7. W. Piyawattanametha, R. P. J. Barretto, T. H. Ko, B. A. Flusberg, E. D. Cocker, H. Ra, D. Lee, O. Solgaard, and M. J. Schnitzer, "Fast-scanning two-photon fluorescence imaging based on a microelectromechanical systems two-dimensional scanning mirror," *Opt. Lett.* **31**, 2018–2020 (2006).
8. J. T. C. Liu, M. J. Mandella, H. Ra, L. K. Wong, O. Solgaard, G. S. Kino, W. Piyawattanametha, C. H. Contag, and T. D. Wang, "Miniature near-infrared dual-axis confocal microscope utilizing a two-dimensional microelectromechanical systems scanner," *Opt. Lett.* **32**, 256–258 (2007).
9. R. Kiesslich, P. R. Galle, and M. Neurath, "Endoscopic surveillance in ulcerative colitis: smart biopsies do it better," *Gastroenterology* **133**, 742–745 (2007).
10. E. H. K. Stelzer and S. Lindek, "Fundamental reduction of the observation volume in far-field light microscopy by detection orthogonal to the illumination axis: confocal theta microscopy," *Opt. Commun.* **111**, 536–547 (1994).
11. E. H. K. Stelzer, S. Lindek, S. Albrecht, R. Pick, G. Ritter, N. Salmon, and R. Stricker, "A new tool for the observation of embryos and other large specimens: confocal theta fluorescence microscopy," *J. Microsc.* **179**, 1–10 (1995).
12. S. Lindek and E. H. K. Stelzer, "Optical transfer functions for confocal theta fluorescence microscopy," *J. Opt. Soc. Am. A* **13**, 479–482 (1996).
13. R. H. Webb and F. Rogomentich, "Confocal microscope with large field and working distance," *Appl. Opt.* **38**, 4870–4875 (1999).
14. T. D. Wang, M. J. Mandella, C. H. Contag, N. Y. Chan, and G. S. Kino, "Dual axes confocal microscope with post-objective scanning and low coherence heterodyne detection," *Opt. Lett.* **28**, 1915–1917 (2003).
15. J. T. C. Liu, M. J. Mandella, S. Friedland, R. Soetikno, J. H. Crawford, C. H. Contag, G. S. Kino, and T. D. Wang, "Dual-axis confocal reflectance microscope for distinguishing colonic neoplasia," *J. Biomed. Opt.* **11**, 054019 (2006).
16. L. K. Wong, T. D. Wang, M. J. Mandella, and G. S. Kino, "Improved rejection of multiply scattered photons in confocal microscopy using dual-axis architecture," *Opt. Lett.* **32**, 1674–1676 (2007).
17. J. A. Izatt, M. R. Hee, G. M. Owen, E. A. Swanson, and J. G. Fujimoto, "Optical coherence microscopy in scattering media," *Opt. Lett.* **19**, 590–592 (1994).
18. J. M. Schmitt, A. Knuttel, and M. Yadlowsky, "Confocal microscopy in turbid media," *J. Opt. Soc. Am. A* **11**, 2226–2235 (1994).
19. M. Kempe, W. Rudolph, and E. Welsch, "Comparative study of confocal and heterodyne microscopy for imaging through scattering media," *J. Opt. Soc. Am. A* **13**, 46–52 (1996).
20. S. M. Mansfield, W. Studenmund, G. S. Kino, and K. Osato, "High numerical aperture lens system for optical storage," *Opt. Lett.* **18**, 305–307 (1993).
21. T. D. Wang, C. H. Contag, M. J. Mandella, N. Y. Chan, and G. S. Kino, "Confocal fluorescence microscope with dual-axis architecture and biaxial postobjective scanning," *J. Biomed. Opt.* **9**, 735–742 (2004).
22. B. W. Pogue and M. S. Patterson, "Review of tissue simulating phantoms for optical spectroscopy, imaging and dosimetry," *J. Biomed. Opt.* **11**, 041102 (2006).

23. L. Henyey and J. Greenstein, "Diffuse radiation in the galaxy," *Astrophys. J.* **93**, 70–83 (1941).
24. A. E. Siegman, *Lasers*, University Science Books, Mill Valley, CA (1986).
25. T. Collier, M. Follen, A. Malpica, and R. Richards-Kortum, "Sources of scattering in cervical tissue: determination of the scattering coefficient by confocal microscopy," *Appl. Opt.* **44**, 2072–2081 (2005).
26. H. J. Wei, D. Xing, G. Y. Wu, H. M. Gu, J. J. Lu, Y. Jin, and X. Y. Li, "Differences in optical properties between healthy and pathological human colon tissues using a Ti:sapphire laser: an *in vitro* study using the Monte Carlo inversion technique," *J. Biomed. Opt.* **10**, 044022 (2005).
27. P. Hsiung, J. Hardy, S. Friedland, R. Soetikno, C. B. Du, A. P. W. Wu, P. Sahbaie, J. M. Crawford, A. W. Lowe, C. H. Contag, and T. D. Wang, "Detection of colonic dysplasia *in vivo* using a targeted fluorescent septapeptide and confocal microendoscopy," *Nat. Methods* **14**, 454–456 (2008).
28. M. Gu, T. Tannous, and J. R. Sheppard, "Effect of an annular pupil on confocal imaging through highly scattering media," *Opt. Lett.* **21**, 312–314 (1996).